ELSEVIER

Spectrochimica Acta Part B 61 (2006) 421 – 432

SPECTROCHIMICA ACTA PART B

www.elsevier.com/locate/sab

Multiplicity and contiguity of ablation mechanisms in laser-assisted analytical micro-sampling☆

Davide Bleiner *, Annemie Bogaerts

PLASMANT Research Group–Dept. of Chemistry, University of Antwerp, Universiteitsplein 1, B-2610 Wilrijk-Antwerp, Belgium

Received 4 October 2005; accepted 17 February 2006
Available online 29 March 2006

Abstract

Laser ablation is implemented in several scientific and technological fields, as well as a rapid sample introduction technique in elemental and trace analysis. At high laser fluence, the ejection of micro-sized droplets causes the enhancement of the surface recession speed and depth resolution degradation as well as the alteration of the sampling stoichiometry. The origin of such large particles seems to be due to at least two different processes, phase explosion and melt splashing. Experimental evidence for both was found in metallic matrices, whereas non-metallic samples showed more complex phenomena like cracking. The spatial distribution of the beam energy profile is responsible for significant differences in the ablation mechanism across the irradiated region and for heterogeneous sampling. Under Gaussian irradiance distribution, the center of the crater, where the irradiance is the highest, experienced a fast heating with rapid ejection of a mixture of particles and vapor (spinodal breakdown). The crater periphery was subjected to more modest irradiation, with melt mobilization and walls formation. The overall resulting particle size distribution was composed of an abundant nano-sized fraction, produced by vapor condensation, and a micro-sized fraction during melt expulsion.

Keywords: Laser ablation; Spinodal breakdown; Melt expulsion; Micro-sampling; Shadowgraphy

1. Introduction

Both in the physical sciences as well as in materials technology, several groups have developed niche-oriented methodologies based on laser irradiation of matter. For instance, in inertially confined fusion (ICF) [1–3], high-power lasers (as alternative to ion beams) are deployed in nuclear fusion reactors to induce heating and compressing of a deuterium and tritium pellet, which can trigger a chain reaction potentially releasing tremendous amounts of energy. In pulsed laser deposition (PLD) [4–6], the vapor induced from a target of known composition is deposited as a stoichiometric thin film upon a substrate. In ion implantation technology, a major advance toward traditional ion-beam facilities is represented by plasma source ion implantation (PSII), where high-power laser ablation-induced plasmas are successfully implemented as ion sources [7]. Further industrial applications include production of nanotubes and nanoparticles, micro-machining, prototyping, cutting, welding and writing [8–16].

Besides, a large number of users turned their attention to laser ablation (LA) because of the clear advantages for solid sample micro-analysis. The often mentioned rapidity, the flexibility to any kind of matrix and the spatially resolved modality have matched more and more to a robust quantification capability [17–24]. Nevertheless, the possibility of quantification without the use of matrix-matched certified reference materials is still under preliminary investigation.

The issue of non-stoichiometric sampling during high-power irradiation has brought more and more attention to the fundamentals of laser-assisted micro-sampling. In the early days, the largest number of publications was devoted to the use of lasers as “black-box” systems for analytical purposes. Recently, more and more papers are devoted to the investigation of laser-induced particle formation, their size distribution and composition [25–35].

☆ This paper was presented at the Colloquium Spectroscopicum Internationale XXXIV, held in Antwerp, Belgium, 4-9 September 2005 and is published in the special issue of Spectrochimica Acta Part B, dedicated to that conference.

* Corresponding author. Tel.: +32 3 820 2383.
E-mail address: davide.bleiner@ua.ac.be (D. Bleiner).

0584-8547/$ - see front matter © 2006 Elsevier B.V. All rights reserved.
doi:10.1016/j.sab.2006.02.007

The questions to address are concerning few critical points, i.e. for a given set of operating conditions (e.g. laser wavelength, pulse duration, pulse spatial and temporal profile, energy, etc.), (i) what is the ablated particle size distribution, (ii) what is the mass ejection rate and (iii) how does each particle composition compare to the parent solid's one. The latter point, i.e. the compositional deviation of the different particle sizes from the original parent solid's stoichiometry, is possibly the most important in analytical chemistry, although from a theoretical point of view this aspect has not been fully addressed, yet.

More in general, the literature mostly offers empirical studies on the effects of laser irradiation and observations on relative ablation products. This heuristic procedure is limited to final-stage perspectives, i.e. what one finds at the end of the experiment. This procedure might be insufficient to unravel the interplaying of the different ablation processes known to take place during the whole duration of the laser pulse as well as in the time after.

Persistent irradiation-induced thermal effects, i.e. activated vaporization and melting, have a key importance. In fact, they are retained to be the pitfall for the majority of applications using LA. For instance, all pure and applied disciplines have major concerns relative to the formation of micron-sized particles, unanimously attributed to the expulsion of melt-related droplets. For non-analytical applications, the fraction of large particles degrading the performance is only the one ejected toward the incoming beam (axial components), because they interfere with the laser processing. In the analytical sciences instead, the entire ejected particle ensemble is important because all particles are carriers of analytical information [25]. The fraction of large melt-derived droplets was reported to decrease as a function of laser irradiance, up to a value of 0.5 GW/cm^2, which is found to be similar to the threshold for plasma shielding [36]. Above this threshold, the particle size distribution remains almost unchanged, but the total number of particles keeps increasing.

The present paper will initially provide a review of all debated mechanisms for LA of both metallic and non-metallic matrices. Subsequently, we will focus on experimental results that give some insights, specifically for the mechanism of ns-LA of metallic matrices. The substantial difference between metallic and non-metallic samples (e.g. glass) in terms of ablation process will also be shown. This motivates the idea of a modeling network specifically for metals, as we are developing [37–39]. In fact, the present discussion will serve as starting point for an ongoing computer simulation study, to investigate LA aerosols in a physical and chemical perspective.

Only short pulse LA (nanosecond regime) is addressed in this work. The reasons for that are two-fold: first, the physical mechanisms that take place in short pulse laser irradiation as well as the typical irradiances are drastically different from those realized in the case of ultra-short LA (femtosecond regime), which need specific treatment. Second, although the use of ns-pulse lasers is sometimes problematic, it is still very popular in the analytical community. For this reason, there is large interest in the fundamental understanding and possibly solving these shortcomings of ns-pulse LA, mostly related to the occurrence of a molten phase. The occurrence of this molten phase and the number of products it brings along is also the subject of this publication.

2. Theoretical background for laser micro-sampling

The laser pulse delivered to the sample interacts with it at different levels: optically (i.e. interband transition, conduction band carrier absorption and defect excitation), thermally (i.e. heat transport and phase change) and also mechanically. The optical penetration depth is defined as the inverse of the absorption coefficient, which is a function of radiation wavelength and material. Assuming a Beer absorption model, it is defined as (symbols are listed in Table 1):

$$\delta = \alpha^{-1}(\lambda) = \frac{z}{\ln\left(\frac{I_0 \cdot (1-\chi)}{I_z}\right)} \tag{1}$$

where it is clear that for $z=\delta$ the intensity I_z has been reduced to $1/e$ of the initial value.

The delivery of laser radiation induces a sudden temperature rise in the electron ensemble, in a measure proportional to the irradiance, i.e. beam power per unit surface. The electron-lattice scattering triggers an energy transfer to the target and over a "long" duration compared to the electron-phonon relaxation time, local thermal equilibrium (LTE) sets in. The relaxation time τ is the reciprocal of the electron-gas' oscillation damping-rate. It can be related to the electrical conductivity measured with DC electric fields, as follows [40] (symbols are listed in Table 1):

$$\tau = \frac{m_e}{e^2 n_e}\sigma \tag{2}$$

For copper, knowing that $\sigma = 6.5\times10^7\ \Omega^{-1}\ \mathrm{m}^{-1}$ and $n_e = 8.5\times10^{28}\ \mathrm{m}^{-3}$ at room temperature [40], one can calculate a relaxation time $\tau_{Cu} = 27$ fs. More in general, the value of τ for metals is typically in the range 10–100 fs. Thus, for ns-pulse irradiation, LTE conditions are correctly assumed and the time-dependent temperature distribution in the target depth can be described by the heat-conduction equation (*Fourier law*), that in one-dimensional form is written as follows (symbols are listed in Table 1):

$$c_p\rho\left(\frac{\partial T(z,t)}{\partial t} - u(t)\frac{\partial T(z,t)}{\partial z}\right) = \frac{\partial}{\partial z}\lambda\frac{\partial T(z,t)}{\partial z} + [1-\chi]\cdot\alpha\cdot I(t)\cdot e^{-\alpha z} \tag{3}$$

where $u(t)$ is the velocity of surface recession per unit pulse, i.e. independent of repetition rate. For non-isotropic condition, the one-dimensional form must me extended to two or three spatial dimensions. The calculated value of $u(t)$ depends on the mechanism(s) taken into account to explain the experimentally observed ablation yield. In the following, the five most frequently debated ablation mechanisms are discussed.

Table 1
Table of symbols used in the equations

Symbol	Description
α	Absorption coefficient
δ	Optical penetration depth
γ	Surface tension
λ	Laser wavelength
ξ	Vaporization coefficient
ρ	Mass density
σ	Electrical conductivity
τ_p	Laser pulse duration
τ	Electron gas relaxation time
Φ	Flux (e.g. vaporization flux)
χ	Target reflectivity
c_p	Heat capacity at constant pressure (units)
D_h	Thermal diffusivity
d_p	Midpoint particle diameter
e	Electron charge
ΔH_v	Enthalpy of vaporization
h	Fluid neck (jet) radius
$I(z,t)$	Beam intensity distribution
J_{het}	Heterogeneous nucleation rate
J_{hom}	Homogeneous nucleation rate
k	Boltzmann constant
m	Atomic/molecular mass
m_e	Atomic/molecular mass
N	Particle collective number
n_{het}	Number density of heterogeneous nuclei
n_{hom}	Number density of homogeneous nuclei
n_e	Number density of electrons
p	Pressure
p_{amb}	Ambient pressure
p_b	Boiling pressure
p_{bub}	Bubble pressure
r_1, r_2	Curvature radii of the fluid neck surface
r_{jet}	Unperturbed fluid neck (jet) radius
r_{part}	Detached particle radius
R	Universal gas constant
t	Time
t_{sat}	Saturation time for homogeneous nucleation
T	Temperature
T_b	Boiling temperature
T_s	Surface temperature
$u(T)$	Surface recession velocity
v	Fluid neck axial velocity
V_c	Bubble critical volume
z	Depth

2.1. Surface vaporization

This process involves an activated migration of surface particles away from the condensed phase into the ambient. It is a necessary condition that the vapor pressure of the condensed phase is lower than the saturated vapor pressure for a given temperature. The rate of vapor pressure change as a function of temperature is given by the well-known Clausius-Clapeyron equation, which determines the so-called binodal line (symbols are listed in Table 1):

$$p(T_s) = p_b \cdot \exp\left[\frac{\Delta H}{R}\left(\frac{1}{T_b}-\frac{1}{T_s}\right)\right] \quad (4)$$

The velocity of surface recession was derived in Ref. [41] from the Hertz-Knudsen equation, inserting Eq. (4) in the pressure term, and multiplying by the vaporization coefficient ξ and the volume m/ρ (symbols are listed in Table 1). After rearranging, the recession velocity is expressed as follows:

$$u(T_s) = \partial z/\partial t = \xi \frac{p_b}{\rho}\sqrt{\frac{m}{2\pi k T_s}} \cdot \exp\left[\frac{\Delta H_v}{R}\left(\frac{1}{T_b}-\frac{1}{T_s}\right)\right] \quad (5)$$

where one notes that the dependency on T_s is not monotone, due to the combined effect of the pre-exponential (*back-flux*) and the exponential term (*forward-flux*). The former term rapidly decreases with T_s and then levels-off at high temperature values, an opposite trend to the exponential term that initially increases and then plateaus. As a combined effect, the forward-flux term dominates at low surface temperature, so that the recession velocity indeed increases with increasing temperature. However, the vaporization process is high-limited and, when the saturation level is reached, the re-condensation term dominates. Thus, at high surface temperatures, the process is increasingly less efficient and, at very high temperature, the surface recession velocity slightly decreases with laser irradiance, as shown before [26].

Recently, Chen and Bogaerts [39] modeled ns-pulse LA assuming normal vaporization of the irradiated sample as the dominating ablation process. They showed that calculated vaporization depths provide a realistic lower-bound to the experimental crater depth, the melt depth they obtained being the upper bound [38]. Depending on the laser irradiance and material thermo-optical properties, the role of vaporization might be more (e.g. Fe) or less (e.g. Al) significant for a given target material.

2.2. Heterogeneous boiling

This process involves an activated migration of particles from the condensed phase into a volatile phase, similarly to surface vaporization, yet the process here occurs within the body of the condensed phase with formation of bubbles. The presence of heterogeneous nuclei disseminated in the irradiated volume should favor the formation of individual bubbles. Indeed, such impurities or defects in the solid are important to lower the activation energy barrier. The bubbles should grow beyond a critical size [26] and coalesce by diffusion, in order to allow extensive boiling [42]. The heterogeneous nucleation rate per unit volume is obtained from the Volumer-Döring formula, as given in the following relation [43] (symbols are listed in Table 1):

$$J_{het} = n_{het} Q \cdot \sqrt{\frac{2\gamma}{\pi \cdot m \cdot F}} \exp\left(-\frac{16\pi\gamma^3 F}{3kT(p_{bub}-p_{amb})^2}\right) \quad (6)$$

where Q and F are two specific control parameters that depend on the geometry of the heterogeneous nuclei. The surface tension γ is a function of temperature, which complicates the application of the equation, but for fast heating rates (10^8 K/s or higher), the surface tension cannot change as a continuum, but step functions should be used. Heterogeneous boiling would be a rapid process, if it would develop under real-world LA

conditions, because it does not require extreme heating levels like are required for homogeneous boiling (see below). However, the process is retained to be not so relevant for short and ultra-short laser ablation ($\tau_p < 50$ ns), because of the low probability of nuclei formation and growth, as well as due to the low bubble diffusion across the melt pool. Moreover, only the very shallow sub-surface region is characterized by the natural occurrence of a significant number of impurities and defects, whose spatial distribution is however limited to few atom layers [44]. Last, in the case of metals, the optical penetration depth is just few tens of nanometers, a depth much thinner than the observed ablated depths per pulse.

2.3. Homogeneous boiling and spinodal breakdown

This process is the explosive boiling of a superheated target material, due to a rapid state-decay, i.e. metastable→unstable→stable, occurring close to the critical temperature. This process leads to the release of a mixture of vapor and droplets that has been also termed "gas of droplets ejection" or "phase explosion".

Fig. 1 shows the T–p phase stability diagram for any arbitrary molten metallic substance. The axes are plotted in terms of reduced temperature and pressure, i.e. relative to the critical point values. The binodal line is the thermodynamic equilibrium boundary that separates coexisting liquid and vapor phase for a given combination of p and T. The binodal line can be rapidly crossed for laser pulses <1 μs, because the induced heating is kinetically too fast. In this situation, a superheated melt is obtained (gray region in Fig. 1), which retains the features of a liquid as long as it is metastable. The limit for metastability is the spinodal line, where the liquid collapses from a metastable into an unstable system.

Actually, approaching the critical point the liquid evolves into an unstable system, i.e. homogeneous nucleation of bubbles is favored. Already at a temperature of $0.8T_c$, one faces an analytical variation of thermophysical properties in the irradiated metal, e.g. decrease of density and electrical

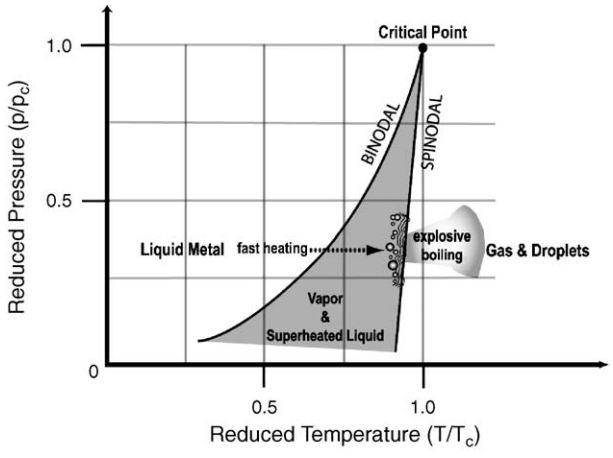

Fig. 1. Phase stability diagram of a liquid metal near the critical point. For fast heating, as obtained during ns LA, the melt can be pushed close to critical conditions (superheating), which favors the realization of explosive boiling.

conductivity, increase of heat capacity, etc. [45,46]. At a temperature of $0.9T_c$, the rate of homogeneous nucleation increases drastically, which leads to phase explosion.

The homogeneous nucleation rate (per unit volume) is given by the following equation [43] (symbols are listed in Table 1):

$$J_{\mathrm{hom}} = n_{\mathrm{hom}} \cdot \sqrt{\frac{2\gamma}{\pi \cdot m}} \exp\left(-\frac{16\pi\gamma^3}{3kT(p_{\mathrm{bub}}-p_{\mathrm{amb}})^2}\right) \quad (7)$$

Martynyuk, the pioneer of phase explosion theory in combination with laser irradiation of metals, reported for Cs a homogeneous nucleation rate of $J = 1\ \mathrm{s}^{-1}\ \mathrm{cm}^{-3}$ at $T/T_c = 0.874$, whereas at $T/T_c = 0.905$ the calculated value was as high as $J = 10^{26}\ \mathrm{s}^{-1}\ \mathrm{cm}^{-3}$ [45,46].

A number of authors [41,47,48] discussed about the time scale for realization of explosive boiling (spinodal breakdown), i.e. the temporal interval it takes to have the irradiated zone filled with homogeneous nucleation bubbles. Knowing the volume of the irradiated zone and the radius of the critical nucleus, one calculates the total number of nuclei. The product $t_{\mathrm{sat}} = 1/(J_{\mathrm{hom}} * V_c)$ gives the time required for saturating the irradiated volume with bubbles based on the nucleation rate and bubble critical volume (for symbols, see Table 1). One should note that the saturation time is independent of total irradiated volume size (or beam spot size), because the bubbles form altogether at the same time. Yet, the total number of nuclei that fill-up the irradiated volume scales up linearly with the size of irradiated volume. Moreover, the size of the critical nuclei is larger for metallic matrices than for non-metallic or organic ones [47], due to better thermal conductivity which favors heat delocalization. This means that a strong superheating regime is required in a metal to induce homogeneous boiling. For a critical bubble radius $r_c = 10$ nm and a homogeneous nucleation rate of $J_{\mathrm{hom}} = 10^{26}\ \mathrm{cm}^{-3}\ \mathrm{s}^{-1}$ [41], one obtains $t_{\mathrm{sat}} = 2.4$ ps, which is in agreement with the time for homogeneous nucleation reported by Rethfeld et al. [48].

There have been several reports on experimental evidences of spinodal breakdown at nanosecond and picosecond pulse length [36,49–52]. Bulgakova as well as the Russo group showed plots with the ablation rate as a function of laser fluence, from where one could see that there is a threshold value for rapid increase of the dependency. This increase is attributed to the transition from a normal vaporization regime into a regime of droplets occurrence.

2.4. Subsurface heating

First Dabby and Paek [53] proposed this process, which puts forward two requirements for a given laser pulse duration: low absorption coefficient and low thermal diffusivity of the target material. The former condition allows volumetric heating of the target material, which can be characterized using the product $K = \alpha^2 D_h \tau_p$ [26]. If the heat that is drawn away during surface vaporization is not rapidly fed-in from the deeper regions, due to low thermal diffusivity, then a temperature gradient develops so that the surface temperature is not the highest. Thus, the

density of the material at depth might become significantly lower than that at the surface and able to induce a convective transport of mass (free convection). Convection might be also become forced if the laser-induced vapor plume exerts a recoil pressure on the surface that plays a significant role in mass mobilization. In either case, mass expulsion should follow in time after the vapor recession.

For instance, the case of graphite and aluminum is here analyzed [49], considering their thermal conductivity (k_{graph}= 0.053 cm^2 s^{-1}, k_{Al}=0.89 cm^2 s^{-1}) and optical absorption coefficient in the UV ($\alpha_{graph}=1.5\times10^5$ cm^{-1}, $\alpha_{Al}=1.5\times10^6$ cm^{-1}). The resulting length of temperature increase beneath the surface (L_{graph}=350 nm, L_{Al}=70 nm) as well as the actual maximum temperature difference (ΔT_{graph}=6200 K, ΔT_{Al}=2 K) show the different behavior for the two typologies of materials and how this process is to be ruled out for the case of metals. In fact, if this process is going to be relevant in terms of material ejection, it could be only so for non-metallic samples and long pulse duration.

2.5. Hydrodynamic instability

The ejection of large droplets depends on both laser irradiance and material properties. The observed increased ablation yield at high laser irradiance is attributed to a transition from a vaporization-dominated ablation regime to a regime where melt-expulsion concurs. Therefore, under such a melt splashing condition, the ablation process becomes more efficient. Voisey et al. [54] have calculated that the energy required to remove material by means of normal vaporization is about four times greater than the energy required to ablate an identical volume with melt ejection.

Splash-related droplet expulsion must be attributed to hydrodynamic instability induced into the melt pool. The origin of such hydrodynamic instability is due to different causes, either external or internal to the sample body. Von Allmen [55] had introduced the concept of "piston effect" operated by the laser pulse, thus invocating an external pressure. This effect was related to 1-D steady state recoil of the plume exerting a pressure back onto the molten surface, which eventually might be inducing a lateral displacement toward the solid edge. It should be said that Von Allmen's work, as well as a number of other papers [56,57], was based on long pulse ablation using IR radiation, where laser-induced melting is known to be extensive.

One problem to the application of this model for short pulse (ns) laser ablation is related to the timing of melt pool onset. Experimental measurements (as also shown here below) showed that plume expansion is several orders of magnitude faster than the beginning of melt displacement. Thus, the potential plume recoil pressure might be indeed exerted upon a still rigid body, which turns into a fluid state only much later on. It seems more likely to claim an energetic internal motor of lateral melt displacement, which is possibly to be related to a sudden expansion during the heating and even the explosive boiling (as explained above). This process might be directly responsible for a vertical ejection of droplet on a fast time scale and indirectly for a radial displacement of molten layers moving along the crater walls and breaking up into droplets under the influence of surface tension.

In fact, melt splashing (Fig. 2) is controlled by a competition between the inertial forces induced by the pressure field into the fluid mass and the surface tension that tends to maintain cohesion. The complexity of finding an appropriate solution to the Navier–Stokes equation for a time-changing volume, whose flow is controlled by increasingly stronger surface forces in proximity of the detachment point, can be overcome using the Lee approximation [59,60]. This approximation is based on space and time dependent fluid neck (or jet, visible in Fig. 2) radius and axial flow velocity (the motion is triggered by the driving pressure on the fluid), as follows (symbols are listed in Table 1):

$$\begin{aligned}&\partial_t h^2+\partial_z(vh^2)=0\\&\partial_t v+v\partial_z v=-\frac{\gamma}{\rho}\partial_z\left(\frac{1}{r_1}+\frac{1}{r_2}\right)+3v\frac{\partial_z(\partial_z vh^2)}{h^2}\end{aligned}\tag{8}$$

The first equation is derived from conservation of mass, reduced to a form that tracks change of radius of the fluid neck (mass density is constant). The second relation comes from the above discussed competition between the inertial force (left side term) and the gradient of surface tension together with the viscous friction (right side terms, respectively).

Such a model has a novel implication for the prediction of particle size distribution, i.e. the intensity of the pressure leading to the jet formation (somehow proportional to the laser irradiance) is of minor relevance during droplet expulsion compared to the surface tension of the molten target material. In this way, the actual size of micro-particles should be nearly independent on laser irradiance and be related to a non-deterministic chaotic process of resonant surface perturbation growth [26].

The size of detached particles can be calculated from volume conservation of the pinching jet as well as surface tension minimization (i.e. the new surface should be as large as

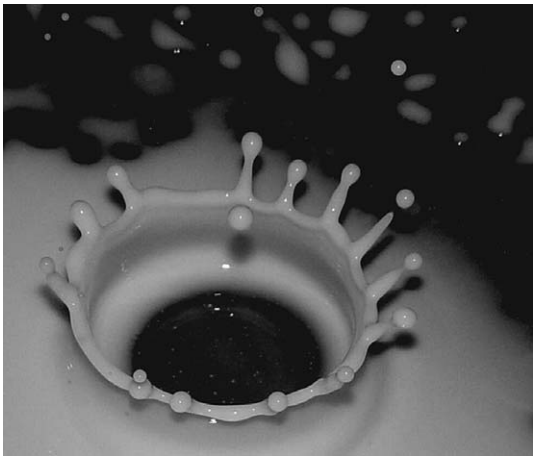

Fig. 2. Schematic visualization of the hydrodynamic evolution of a fluid system under and impulse stress (here milk). Note the non-deterministic formation of jets at the sides and their break-up into droplets. From Ref. [58].

possible). Here the theory predicts that the radius of a forming particle must be larger than the jet radius by at least 50%, i.e. $r_{part} > 1.5 r_{jet}$ [59]. Thus, the system tends preferentially to the production of a small number of large particles. This size–number relation is important and opposite to the one valid for nano-sized particles formed by vapor condensation. In the latter case, one observes a large number of preferentially small size, i.e. with positive skew of the size distribution (see also measurement shown below).

3. Experimental

Several measurements were conducted to investigate the characteristics of the melt ablation products, which are presented and discussed in the next section. Detailed inspection of the crater morphology and particles was done to obtain information on the melt pool evolution. Individual laser-induced particles were observed using secondary electron images. Time-resolved acquisitions of the ejection products were possible by means of shadowgraphy. Particle size distribution (PSD) was determined in the range 10 nm–1 μm using a differential mobility analyzer.

The laser ablation system used is based on the Quanta-Ray DCR-11 (Spectra-Physics, Germany), but it was in-house modified from the commercial 1064 nm Nd:YAG. The output mirror of the cavity was a curved one to obtain an 'unstable resonator' type cavity, which provided high output power (fluence in this work was 20 J/cm^2) because a wider region of the YAG crystal was excited. This led to a non-uniform spatial beam profile (Bessel or so-called "donut profile"). The frequency-quadrupled wavelength (266 nm, Q-switched with 6 ns pulse length) was generated with two KDP's crystals set along the beam path. The beam was pulsed at 10 Hz and a 150-μm spot size was obtained using a 40-mm focal distance objective lens. The ablation cell was a 30-cm^3 cylindrical cell filled with alternatively argon, helium, nitrogen, air or sulfur-hexafluoride, though here only most relevant results will be shown. Sulfur-hexafluoride induced intense shielding of the laser radiation, due to gas dissociation, and hence the ablation craters were always unaccented.

The sample was micro-machined to visualize inner structures of ablation products. A Strata DB 235 dual beam focused ion beam (FIB) workstation (*FEI Company*, USA) was used that incorporates a FIB and a scanning electron microscope (SEM) column tilted to each other at an angle of 52°. The FIB column is adjustable from 1 pA to 20,000 pA at 30 kV with a specified resolution of 7 nm, as given by the manufacturer. The instrument is equipped with four secondary electron and ion detectors.

In the shadowgraphy set-up, two beams were used, i.e. so-called pump–probe approach. The pump was a XeCl excimer laser (wavelength 308 nm, pulse width FWHM 25 ns) with output energy of 75 mJ, though an attenuator was used along the beam path to adjust the energy delivered onto the sample. The probe beam was the second harmonic of Nd:YAG (λ=532 nm, τ_p=6 ns) and it was used to induce fluorescence in a water-diluted dye (Rhodamine 6G) in a quartz cuvette. The dye was chosen as one being characterized by a strong fluorescence band in the spectral range of the working wavelength (λ>480 nm). The direction cuvette–CCD camera was congruent with the sample surface orientation and orthogonal to the pump beam. Upon ablation, the released matter as well as the induced shockwave caused a local difference of the ambient gas refractive index that could be acquired with the CCD camera. In this very set-up, the sample was mounted inside a gastight chamber so that a controlled atmosphere could be formed. Several gases were used, but in this paper results for argon are presented. Further information on the set-up is available in the literature [61,62].

PSDs were acquired using a differential mobility analyzer (DMA). A radioactive unit charges the aerosol particles and depending on the voltage applied particles of matching charge-to-surface ratio are gated into the condensation particle counter (CPC). Being the total charge constant, the ratio gives information on the size of the particles, under the assumption of identical particle shape. This technique is suited for the determination of sizes in the range 10 nm–1 μm [63].

4. Results and discussion

4.1. Ablation crater morphology

The inspection of the ablation products morphology provided information on the mechanisms of formation. In the case of metallic samples, a relatively low melting point favors the prompt formation of a fluid phase, which under the action of intense pressure is mobilized. Hence, one observes a modification of the surface topography in the neighborhood of the ablation crater, whose roughness is a function of laser energy and material's thermophysical properties. Fig. 3 shows a selection of measured craters from ablated copper and silicon with identical laser setting.

The crater in copper (Fig. 3A,B) is characterized by steep contacts between the bottom and the wall, which is typical for ablation above the threshold. The crater bottom (shown in more detail in Fig. 4A) was somehow rough, which is an effect partially due to the non-homogenized spatial beam profile and partially due to the material ejection mechanism. It showed a wavy structure with thin filaments collapsed on one side and intertwined. The wall of the copper crater (see Fig. 3A) showed several sheets piled-up on their move toward the edge, where there are signs of overflow and tiny tips. The structure would suggest a laminar flow in a viscous confined regime. On the forefront of these laminae, the flow breaks up into a turbulent regime as also shown below in cross-section images of the crater walls (Fig. 6).

The crater in silicon (Fig. 3C,D) showed even steeper edges than the copper sample. The wall was made-up of a number of columnar structures in close contact one another. The surface of these filaments was characterized by the presence of fine-structured ripples (shown in more detail in Fig. 4B). Micron-sized particles were observed in the immediate proximity, right outside the crater (Fig. 3C,D).

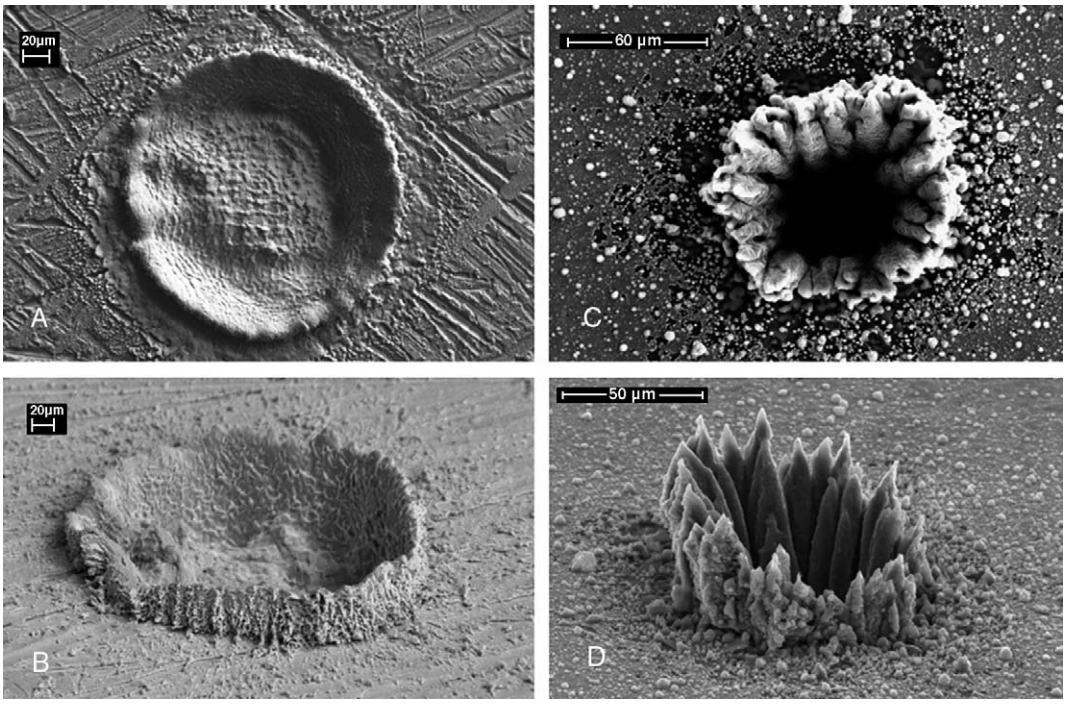

Fig. 3. Crater structures obtained with Nd:YAG laser at 266 nm, 4 mJ, 10 Hz. (A, B) copper and (C, D) silicon.

The observed structure would suggest a rapid and intense normal transport of material in the center part of the crater. A more sluggish radial displacement could be inferred next to the wall. This scheme would suggest a strong irradiation regime in the center and more modest irradiation at the periphery. This might be explained with the spatial beam profile, as schematically explained in Fig. 5.

In this case, the center would be heated-up at an extreme rate possibly inducing explosive boiling, whereas the sides would experience more soft energy deposition due to lower fluence upon inclined crater walls, thus just triggering melting and hydrodynamic mobilization. The attainment of a phase explosion stage would contribute to a rapid and persistent removal of material in the form of "gas of droplets", leaving a set of casts due to the strong vertical acceleration on the crater bottom. Hydrodynamic instabilities in the mobile melt phase at the sides would less efficiently produce a low number of large particles by means of jet break-up.

Fig. 6 shows two cross sections of the crater wall obtained using FIB. This facility allowed micro-machining the sample and in this case it was used to dig a trench across the crater wall and have SEM images of the inner structure. Fig. 6C shows the same region of Fig. 6B, eroded further ahead. One notes the occurrence of several overlapping layers and the presence of cavities in the bulk of the crater wall, which would rule out the presence of a laminar flow regime. Such cavities have a complex geometric shape as can be inferred from a comparison

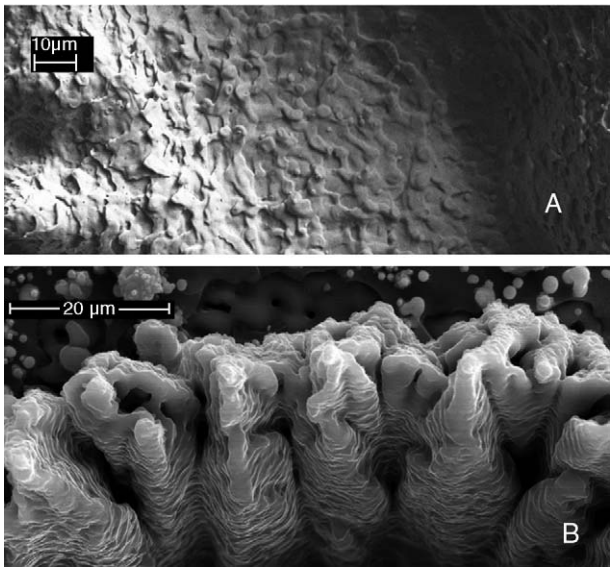

Fig. 4. Detailed view of the crater fine structure of Fig. 3. (A) Crater bottom in copper and (B) crater wall in silicon.

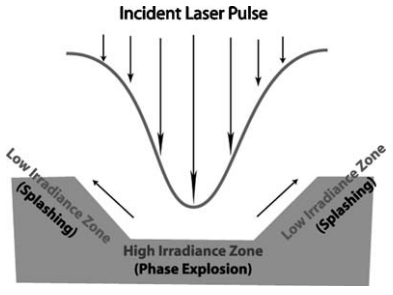

Fig. 5. Schematic of beam profile and irradiance in adjacent zones of the crater. The center is characterized by a stronger heating regime and therefore explosive boiling. The sides are characterized by a weaker heating regime, which might be sufficient to initiate the splashing phenomena.

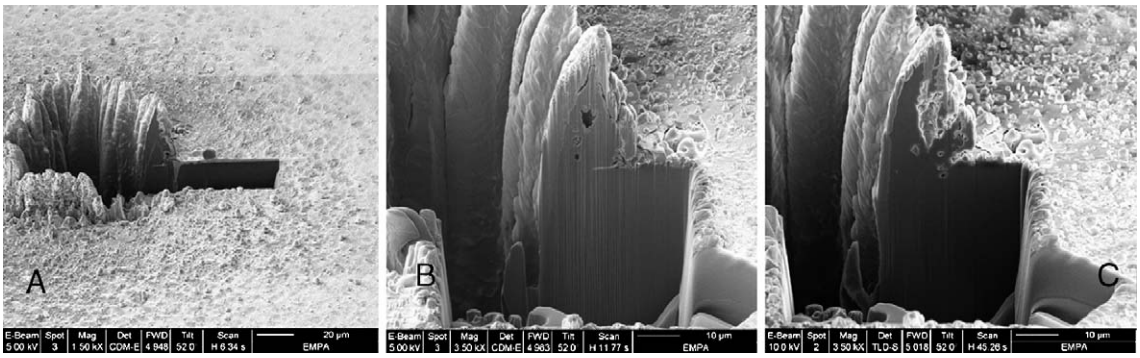

Fig. 6. Cross section of the crater wall in silicon shown in Fig. 3. The occurrence of voids and the presence of overlapping layers suggest a stage of melt mobilization.

between the two planar sections. Inspection of the cross sections showed that voids, ripples and bends were occurring extensively, which is possibly a consequence of melt mobilization. It demonstrates that the flow is not laminar like in the upstream regions inside the crater. The information obtained is that there is a transition region from laminar to turbulent flow, due to a sudden increase of the velocity at the crater rims.

4.2. Material ejection

Under this scheme, the ablation processes are spatially separated because of the heterogeneous energy delivery across the irradiated surface. Further observations, as shown below, indicated that the ejection of material in the center was also temporally separated from the one along the margin. This would indeed support the idea of a fast catastrophic phase-explosion stage, where time lag to achieve critical conditions is reported in ref. [47] as 5.5 ns and approximately 10 ps in Ref. [48] for its completion, and a late-coming melt splashing stage on a time-scale of few microseconds [64].

Indeed, shadowgraphy measurements permitted to observe the release of two temporally distinct batches of material, as shown in Fig. 7. Fig. 7A,B are two snapshots obtained from the ablation of silicon, whereas Fig. 7C,D were obtained with the same laser system, ablating tin. Here, the sample is on the right side and the laser beam (the pump beam at 308 nm) is coming from the left side of the images.

In Fig. 7A, one clearly sees the trace of a spherical shockwave as it appears at 200 ns after the delivery of the pulse. A further snapshot acquired at 4 μs permitted to evaluate the outward expansion, which is shown in Fig. 7B. In both images, i.e. at a time delay of 0.2 as well as 4 μs, the shockwave

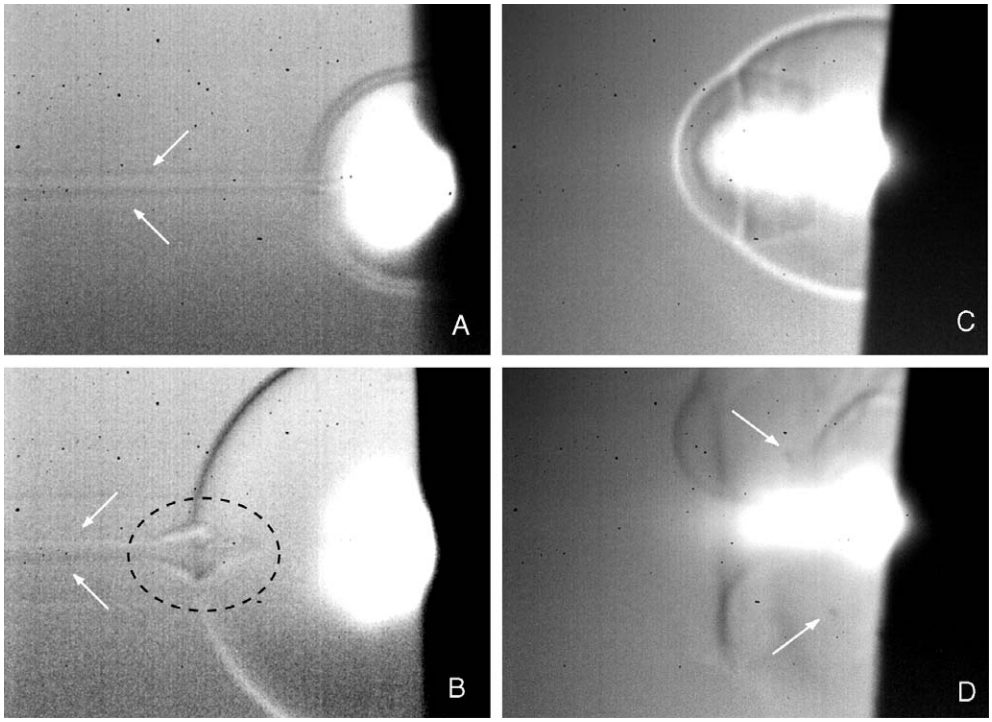

Fig. 7. Material ejection timing as visualized with shadowgraphy (see Section 3 for conditions). Ablation in silicon is here observed at 0.2 μs (A) and 4 μs (B) after the end of the pulse. Note the rapid center expulsion of matter that at 4 μs is still visible. Ablation in tin is here observed at 0.2 μs (C) and 1 μs (D). Due to the low melting point of this material, a dense cloud of large particles is observed at the sides.

is penetrated by a column of material ejected normal to the surface (see the arrows) moving faster than the shockwave itself. The emission of such material was a function of laser fluence. The emission was very rapid and lasted for several microseconds. In Fig. 7B, the formation of a wake at the shockwave front edge is seen, as highlighted by the circle.

In Fig. 7C, one sees the expanding shockwave at 200 ns after the laser irradiation of tin. Tin is characterized by a very low melting point (i.e. T_m(Sn)=232 °C) compared to other pure substances used in this work (e.g. T_m(Cu)=1083 °C, T_m(Si) =1410 °C) and hence permitted optimal visualization of the melt expulsion process. In Fig. 7D, one notes the emission of a second batch of material that was initiated not before 1 μs after the pulse delivery. These particles diffused along whirling trajectories as could be observed in a series of snapshots obtained at 50 ns time delay and were located at the opposite sides of the ablation crater. The arrows highlight some bigger particles. The Russo group [64] has shown previously the ejection of large particles from brass, on a similar time-scale. The observation of distinct laser-induced particulate batches supports the thesis of multiple co-existing ablation mechanisms at high irradiance condition.

4.3. Particle characteristics

Further information on the ablation mechanism can be obtained by the investigation of the particulate produced. Recently, several publications addressed this topic. The Günther group [28–30] has investigated extensively the laser-induced particle size distribution (PSD) from the ablation of NIST 610s glasses under several operating conditions. The PSD was found to change significantly from shallow to deep crater ablation, namely the ratio large/small particles decreased by a factor of 3 over 1-min ablation at 10 Hz. This would indicate that the mechanism of ablation is very different at different crater depths, i.e. at large depth the large particle expulsion process is less efficient.

This was also demonstrated by the observation that laser ablation with a scanning mode (so-called “raster ablation”) provided steady aerosol characteristics, though with a certain dependency on the translation speed. Only by ablating on a fixed position (so-called “point ablation”), they observed an evolution of the aerosol mean size.

The same authors showed a drastic dependency of the PSD on the radiation wavelength. They reported that, only with λ=213 nm and λ=266 nm particles larger than 150 nm formed, whereas with λ=193 nm (obtained from the same solid-state laser system using an optical parametric oscillator), all particles they found were <150 nm: a monodisperse aerosol with mode at approximately 80–90 nm. Furthermore, they confirmed that large and small particles have heterogeneous composition, where elements like Cu, Zn, Ag, Tl, Pb and Bi were found to be enriched in the smaller fractions as high as 90% relative to Ca. In any case, the overall composition of small and large particles was found to match with the original sample composition.

Koch et al. [34] determined the size distribution on a brass sample using a near-IR femtosecond laser. For a fluence below 5 J/cm^2, they found a 10±35 nm monodisperse aerosol of stoichiometric composition, whereas at 10 J/cm^2 the results showed a bimodal size distribution with modes at 20±50 nm and 1±5 μm and non-stoichiometric composition. A comparison with ns ablation showed more pronounced formation of micro-sized particles that more strongly deviate from the stoichiometry of the irradiated solid. In a recent work, Koch et al. [65] investigated non-conducting samples using the same facility and they found an opposite scheme as compared to the investigations on brass. In fact, for a fluence higher than 5 J/cm^2, the overall aerosol composition matched with the parent material within a 10% deviation. For a lower fluence, a more significant compositional deviation from the parent material was found. The major fraction of the aerosol mass was in the 10–100 nm range and the relative abundance of micro-sized particles has been found to diminish with high fluence.

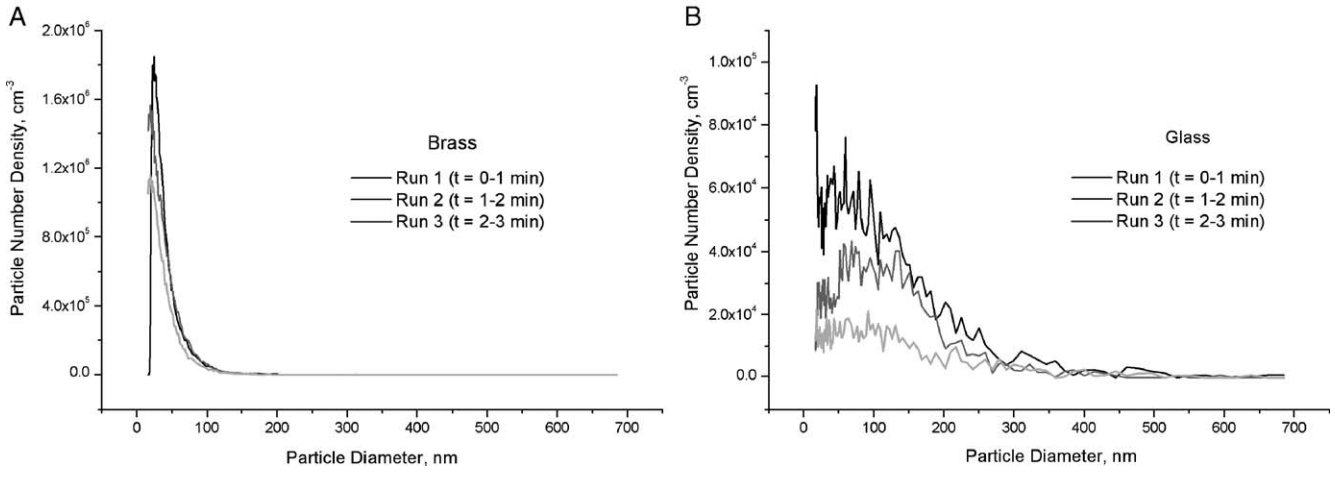

Fig. 8. Particle size distribution obtained for the ablation of brass (A) and glass NIST 610 (B), under conditions reported in the experimental section. Each run (1 min long) showed a sensible decrease of the integrals. The figures show that metal and non-metal matrices behave differently upon laser ablation (see also Fig. 9).

Kosler et al. [66] have also investigated the laser-induced aerosol from NIST silicate glasses. In the initial stages of ablation, multi-modal particle sizes <2.5 μm were found, whose span reduced to <0.3 μm after ca. 30 s ablation. The big particles found were spherical or elongated, whereas small particles are clusters enriched in Pb vs. U.

Liu et al. [33] investigated size-related effects on the ICP-MS signal from brass samples. They found that Cu partitioned in the melt-related particulate, whereas Zn was more prone to enrich in the nano-particulate.

Our own DMA measurement results are shown in Fig. 8. The number density is plotted on the vertical axis and it was calculated as dN/d log(d_p) as fully explained in ref. [63]. One notes that the PSD under identical irradiation conditions is very different for a non-metallic and metallic sample. In the latter, a smooth and relatively narrow distribution curve, with positive skew, showed a mode at about 30 nm (formed by vapor condensation). In the case of glass, the profile is more jagged and wide, possibly due to deeper volumetric absorption of radiation as well as due to fractures induced in the material (shown in Fig. 9) contributing to mechanical spallation [67].

This observation imposes to make a clear distinction of the two cases, i.e. metallic and non-metallic matrices, when trying to develop a numerical model for laser ablation particulate formation. Fig. 8 shows also the evolution of the PSD with ablation time, where three sequential 1-min runs are plotted. The mode in the brass sample shifts toward finer size as a function of ablation time and, apparently, it is soon outside the measurement window (i.e. below 10 nm), indicating that for deep craters the extracted aerosol was just the finer fraction. For the glass sample, the time-dependent size shift was not so evident, but one observes a significant reduction of ablated mass, probably due to in-crater trapping, as shown in Fig. 9. This reduction is also shown by the metallic sample, though to a more modest extent.

This would suggest that, under identical duration of irradiation, the surface recession depth is more modest for the metallic sample. This is in agreement with theoretical considerations on optical penetration depth for metal and glass: δ_{Cu}=13 nm and δ_{SiO_2}(glass) =21 μm (recalculated from original data of extinction coefficients in Ref. [68]).

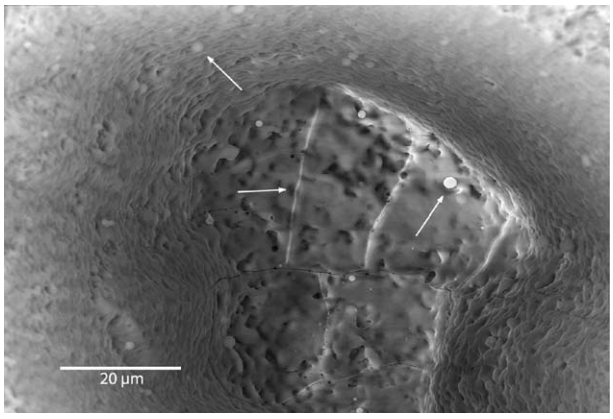

Fig. 9. SEM image showing fractures inside the glass crater at the bottom. Note also the trapping of large spherical particles inside the edges. LA conditions as given in Section 3.

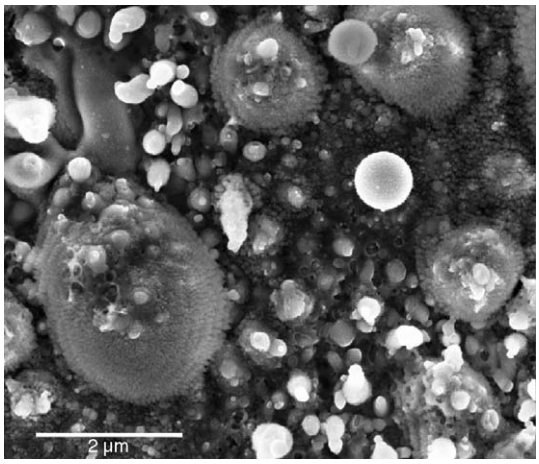

Fig. 10. SEM image showing a survey of particles produced during laser ablation in silicon (conditions given in the experimental section). One note large melt-derived particles produced by droplet expulsion as well as finer particulate produced by vapor condensation.

Finally, Fig. 10 shows a group of laser-induced particles as they were observed on the sample surface. One notes that the coarser particles have a smooth surface and shapes variable between the sphere and a prolate ellipsoid, suggesting tensile stresses. These morphologies are to be attributed to the temperature at time of detachment: if the droplet was still fully molten upon detachment then its fluidity would allow reshaping a minimum surface-to-volume geometry, i.e. a sphere; otherwise a nearby quenching droplet retained the wobbling elongated morphology produced during jet pinching-off. As discussed elsewhere [69], particles might also build fractal clusters by adhesion of nano-particulate on the surface of large droplets. Nanoparticles can be seen in Fig. 10 on the background. This fraction of particles resulted from condensation of vapor and are therefore enriched in volatile elements as mentioned above.

5. Conclusions

Five potential material removal mechanisms have been discussed together with their applicability for short pulse laser ablation of metallic matrices. Results indicated that a number of processes interlace during the material irradiation time and in the subsequent time. It was possible to show that a few of them might be co-existing for high fluence irradiation of metals when the beam profile is not homogenized, i.e. spinodal breakdown and hydrodynamic expulsion. Binodal (surface) vaporization is active as well, but it is retained to be the dominating ablation mechanism at low fluence regime, i.e. below the droplet formation threshold, and at saturated flux rates for high power LA.

This work showed evidences of spatial and temporal separation of the dominating ablation processes. Such separations are attributed to the spatial beam profile as well as the time required for explosive boiling and the melting to realize in the given sample.

Spinodal breakdown is a fast and catastrophic process that is initiated by homogeneous boiling shortly before the critical point. This process leads to a mixture of vapor and melt droplets ejected normally from the crater bottom.

Hydrodynamic expulsion, or "splashing", is controlled by a competition between the inertial forces induced by the pressure field into the viscous melt and the surface tension that tends to maintain cohesion. The size–number relation of formed particles suggests that micro-particles tend to be as large as possible to minimize surface tension and low in number, as also shown from measurements of PSDs. This behavior is opposite for nano-size particulate produced by vapor condensation. Jet break-up and droplets fission is a non-linear process, obtained by a competition among resonant surface vibrations and cohesive surface tension. It should be pointed out that the properties of materials are non-standard under superheated conditions, which makes the task of developing a modeling network non-trivial.

Computational studies are indeed required to unraveling the interplaying mechanisms and providing guidelines for future better performance in many applied fields of laser ablation. Therefore, the authors are committed with the development of a numerical model that would address the open issue on size distribution and composition of a given combination laser beam and metallic sample.

Acknowledgements

Th. Lippert and G. Koptivitas (Paul Scherer Institute, Switzerland) are acknowledged for the shadowgraphy determinations. Ph. Gasser, P. Lienemann, M. Trottmann, U. Lehmann and D. Schreiber (EMPA, Switzerland) are acknowledged for support with the SEM, FIB and DMA acquisitions. Mrs. Ch. Surber and Mr. J. Glas of the EMPA-EAWAG library are acknowledged for assistance in literature searches. Z. Chen (G. Washington University), D. Autrique (Universiteit Antwerpen) and G. Müller (ThyssenKrupp Stahl, Germany) are acknowledged for discussions. D. Bleiner is financed by the Flemish FWO Fund for Scientific Research.

References

[1] C. Labaune, J. Fuchs, S. Depierreux, H.A. Baldis, D. Pesme, J. Myatt, S. Hüller, V.T. Tikhonchuk, G. Laval, Laser-plasma interaction physics in the context of fusion, C. R. Acad. Sci. Paris, Ser. I 6 (2000) 727–735.

[2] M.J. van der Wiel, P.W. van Amersfoort, A role for free electron lasers in fusion? Fusion Eng. Des. 11 (1989) 245–253.

[3] D.H.H. Hoffmann, R. Bock, A.Ya Faenov, U. Funk, M. Geissel, U. Neuner, T.A. Pikuz, F. Rosmej, M. Roth, W. Süß, N. Tahira, A. Tauschwitz, Plasma physics with intense laser and ion beams, Nucl. Instrum. Methods Phys. Res. B 161–163 (2000) 9–18.

[4] D.B. Chrisey, G.K. Hubler (Eds.), Pulsed Laser Deposition of Thin Films, Wiley-Interscience, New-York, 1994.

[5] P.R. Willmott, Deposition of complex multielemental thin films, Prog. Surf. Sci. 76 (2004) 163.

[6] L.A. Greer, M.D. Tabat, C. Lu, Future trends for large-area pulsed laser deposition, Nucl. Instrum. Methods Phys. Res. B 121 (1997) 357.

[7] D. Bleiner, F. Belloni, D. Doria, A. Lorusso, V. Nassisi, Overcoming pulse mixing and signal tailing in laser ablation inductively coupled plasma mass spectrometry depth profiling, J. Anal. At. Spectrom. 20 (2005) 1337–1343.

[8] F. Kokai, A. Koshio, M. Shiraishi, T. Matsuta, S. Shimoda, M. Ishihara, Y. Koga, H. Deno, Modification of carbon nanotubes by laser ablation, Diamond Relat. Mater. 14 (2005) 724–728.

[9] C.D. Scott, S. Arepalli, P. Nikolaev, R.E. Smalley, Growth mechanisms for single-wall carbon nanotubes in a laser-ablation process, Appl. Phys. A Mater. Sci. Process. 72 (2001) 573–580.

[10] F. Huisken, H. Hofmeister, B. Kohn, M.A. Laguna, V. Paillard, Laser production and deposition of light-emitting silicon nanoparticles, Appl. Surf. Sci. 154–155 (2000) 305–313.

[11] H. Cai, N. Chaudhary, J. Lee, M.F. Becker, J.R. Brock, J.W. Keto, Generation of metal nanoparticles by laser ablation of microspheres, J. Aerosol Sci. 29 (1998) 627–636.

[12] M.F. Becker, J.R. Brock, Hong Cai, D.E. Henneke, J.W. Keto, Jaemyoung Lee, W.T. Nichols, H.D. Glicksman, Metal nano-particles generated by laser ablation, Nanostruct. Mater. 10 (1998) 853–863.

[13] S. Nikumb, Q. Chen, C. Li, H. Reshef, H.Y. Zheng, H. Qiu, D. Low, Precision glass machining, drilling and profile cutting by short pulse lasers, Thin Solid Films 477 (2005) 216–221.

[14] M.S. Amer, M.A. El-Ashry, L.R. Dosser, K.E. Hix, J.F. Maguire, B. Irwin, Femtosecond versus nanosecond laser machining: comparison of induced stresses and structural changes in silicon wafers, Appl. Surf. Sci. 242 (2005) 162–167.

[15] J.Y. Cheng, C.W. Wei, K.H. Hsu, T.H. Young, Direct-write laser micromachining and universal surface modification of PMMA for device development, Sens. Actuators B, Chem. 99 (2004) 186–196.

[16] H.J. Booth, Recent applications of pulsed lasers in advanced material processing, Thin Solid Films 453–454 (2004) 450–457.

[17] D. Günther, B. Hattendorf, Solid sample analysis using laser ablation inductively coupled plasma mass spectrometry, TrAC, Trends Anal. Chem. 24 (2005) 255–265.

[18] K. Meissner, T. Lippert, A. Wokaun, D. Günther, Analysis of trace metals in comparison of laser-induced breakdown spectroscopy with LA-ICP-MS, Thin Solid Films 453–454 (2004) 316–322.

[19] J.S. Becker, Applications of inductively coupled plasma mass spectrometry and laser ablation inductively coupled plasma mass spectrometry in materials science, Spectrochim. Acta Part B 57 (2002) 1805–1820.

[20] W.E. Halter, Th. Pettke, Ch.A. Heinrich, B. Rothen-Rutishauser, Major to trace element analysis of melt inclusions by laser-ablation ICP-MS: methods of quantification, Chem. Geol. 183 (2002) 63–86.

[21] J. Feldmann, A. Kindness, P. Ek, Laser ablation of soft tissue using a cryogenically cooled ablation cell, J. Anal. At. Spectrom. 17 (2002) 813–818.

[22] R.J. Watling, B.F. Lynch, D. Herring, Use of laser ablation inductively coupled plasma mass spectrometry for fingerprinting scene of crime evidence, J. Anal. At. Spectrom. 12 (1997) 195–203.

[23] T. Oguri, H. Inoue, S. Tsuge, K. Kitagawa, N. Arai, Laser ablation-assisted radiofrequency atomization excitation source for direct determinations of elements in ceramics, J. Anal. At. Spectrom. 12 (1997) 823–826.

[24] L. Balcaen, J. Lenaerts, L. Moens, F. Vanhaecke, Application of laser ablation inductively coupled plasma (dynamic reaction cell) mass spectrometry for depth profiling analysis of high-tech industrial materials, J. Anal. At. Spectrom. 20 (2005) 417–423.

[25] D. Bleiner, P. Lienemann, H. Vonmont, Laser-induced particulate as carrier of analytical information in LA-ICPMS direct solid microanalysis, Talanta 65 (2005) 1286–1294.

[26] D. Bleiner, Mathematical modelling of laser-induced particulate formation in direct solid microanalysis, Spectrochim. Acta Part B 60 (2005) 49–64.

[27] I. Horn, D. Günther, The influence of ablation carrier gasses Ar, He and Ne on the particle size distribution and transport efficiencies of laser ablation-induced aerosols: implications for LA–ICP–MS, Appl. Surf. Sci. 207 (2003) 144–157.

[28] M.l. Guillong, H.-R. Kuhn, D. Günther, Application of a particle separation device to reduce inductively coupled plasma-enhanced elemental fractionation in laser ablation-inductively coupled plasma-mass spectrometry, Spectrochim. Acta Part B 58 (2003) 211–220.

[29] M. Guillong, D. Günther, Effect of particle size distribution on ICP-induced elemental fractionation in laser ablation-inductively coupled plasma-mass spectrometry, J. Anal. At. Spectrom. 17 (2002) 831–837.
[30] M. Guillong, I. Horn, D. Günther, A comparison of 266 nm, 213 nm and 193 nm produced from a single solid state Nd:YAG laser for laser ablation ICP-MS, J. Anal. At. Spectrom. 18 (2003) 1224–1230.
[31] Zs. Márton, L. Landström, M. Boman, P. Heszler, A comparative study of size distribution of nanoparticles generated by laser ablation of graphite and tungsten, Mater. Sci. Eng., C 23 (2003) 225–228.
[32] J. Kosler, M. Wiedenbeck, R. Wirth, J. Hovorka, P. Sylvester, J. Míková, Chemical and phase composition of particles produced by laser ablation of silicate glass and zircon—implications for elemental fractionation during ICP-MS analysis, J. Anal. At. Spectrom. 20 (2005) 402–409.
[33] C.Y. Liu, X.L. Mao, J. González, R.E. Russo, Study of particle size influence on laser ablation inductively coupled plasma mass spectrometry using an in-line cascade impactor, J. Anal. At. Spectrom. 20 (2005) 200–203.
[34] J. Koch, A. von Bohlen, R. Hergenröder, K. Niemax, Particle size distributions and compositions of aerosols produced by near-IR femto-and nanosecond laser ablation of brass, J. Anal. At. Spectrom. 19 (2004) 267–272.
[35] H.R. Kuhn, D. Günther, Laser ablation-ICP-MS: particle size dependent elemental composition studies on filter-collected and online measured aerosols from glass, J. Anal. At. Spectrom. 19 (2004) 1158–1164.
[36] J.H. Yoo, S.H. Jeong, X.L. Mao, R. Greif, R.E. Russo, Evidence for phase-explosion and generation of large particles during high power nanosecond laser ablation of silicon, Appl. Phys. Lett. 76 (2000) 783–785.
[37] A. Bogaerts, Z. Chen, R. Gijbels, A. Vertes, Laser ablation for analytical sampling: what can we learn from the modeling? Spectrochim. Acta Part B 58 (2003) 1867–1893.
[38] A. Bogaerts, Z. Chen, Effect of laser parameters on laser ablation and laser-induced plasma formation: a numerical modeling investigation, Spectrochim. Acta Part B 60 (2005) 1280–1307.
[39] Z. Chen, A. Bogaerts, Laser ablation of Cu and plume expansion into 1 atm ambient gas, J. Appl. Phys. 97 (2005) 063305.
[40] M. Fox, Optical Properties of Solids, Oxford University Press, 2001.
[41] A. Miotello, R. Kelly, Critical assessment of thermal models for laser sputtering at high fluences, Appl. Phys. Lett. 67 (1995) 3535–3537.
[42] S.G. Kandlikar, M. Shoji, V.K. Dhir (Eds.), Handbook of Phase Change Taylor and Francis Group, 1999.
[43] M. Blander, J.L. Katz, Bubble nucleation in liquids, Am. Inst. Chem. Eng. (AIChE J.) 21 (1975) 833–848.
[44] H. Kleinert, Gauge Fields in Condensed Matter, vol. II, 1997, pp. 743–1456.
[45] M.M. Martynyuk, Phase explosion of a metastable fluid, Combust. Explos. Shock Waves 13 (1978) 178–191.
[46] M.M. Martynyuk, Critical point parameters of metals, Russ. J. Phys. Chem. 57 (1983) 810–821.
[47] X. Xu, Phase explosion and its time lag in nanosecond laser ablation, Appl. Surf. Sci. 197–198 (2002) 61–66.
[48] B. Rethfeld, K. Sokolowski-Tinten, D. von der Linde, S.I. Anisimov, Ultrafast thermal melting of laser-excited solids by homogeneous nucleation, Phys. Rev. B 65 (2002) 092103.
[49] N.M. Bulgakova, A.V. Bulgakov, Pulsed laser ablation of solids: transition from normal vaporization to phase explosion, Appl. Phys. A 73 (2001) 199.
[50] D.B. Geoghan, Imaging and blackbody emission spectra of particulates generated in the KrF-laser ablation of BN and $YBa_2Cu_3O_{7-x}$, Appl. Phys. Lett. 62 (1993) 1463–1465.
[51] K.H. Song, X. Xu, Explosive phase transformation in excimer laser ablation, Appl. Surf. Sci. 127–129 (1998) 111.
[52] R.E. Russo, X.L. Mao, C. Liu, J. Gonzalez, Laser assisted plasma spectrochemistry: laser ablation, J. Anal. At. Spectrom. 19 (2004) 1084–1089.
[53] F.W. Dabby, U. Paek, High-intensity laser-induced vaporization and explosion of solid material, IEEE J. Quantum Electron. QE-8 (1972) 106–111.
[54] K.T. Voisey, S.S. Kudesia, W.S.O. Rodden, D.P. Hand, J.D.C. Jones, T.W. Clyne, Melt ejection during laser drilling of metals, Mater. Sci. Eng. A 356 (2003) 414.
[55] M. Von Allmen, Laser drilling velocity in metals, J. Appl. Phys. 47 (1976) 5460–5463.
[56] C. Chan, J. Mazumder, One-dimensional steady-state model for damage by vaporization and liquid expulsion due to laser-material interaction, J. Appl. Phys. 62 (1987) 4579–4586.
[57] R.K. Ganesh, A. Faghri, Y. Hahn, A generalized thermal modeling for laser drilling process: I. Mathematical modeling and numerical methodology, Int. J. Heat Mass Transfer 40 (1997) 3351.
[58] Dror-Bar Natan, http://www.math.toronto.edu/~drorbn/Gallery/Misc/MilkDrops/index.html.
[59] J. Egger, Nonlinear dynamics and breakup of free-surface flows, Rev. Mod. Phys. 69 (1997) 865.
[60] J. Eggers, Tropfenbildung, Phys. Bl. 53 (1997) 431–434.
[61] M. Hauer, D.J. Funk, Th. Lippert, A. Wokaun, Time-resolved techniques as probes for the laser ablation process, Opt. Lasers Eng. 43 (2005) 545–556.
[62] M. Hauer, D.J. Funk, Th. Lippert, A. Wokaun, Time resolved study of the laser ablation induced shockwave, Thin Solid Films 453–454 (2004) 584–588.
[63] P. Baron, K. Willeke, Aerosol Measurement: Principles, Techniques, and Application, Wiley-Interscience, 2001.
[64] R.E. Russo, X.L. Mao, H.C. Liu, J.H. Yoo, S.S. Mao, Time-resolved plasma diagnostics and mass removal during single-pulse laser ablation, Appl. Phys., A Mater. Sci. Process. 69 (1999) S887–S894.
[65] J. Koch, H. Lindner, A. von Bohlen, R. Hergenröder, K. Niemax, Elemental fractionation of dielectric aerosols produced by near-infrared femtosecond laser ablation of silicate glasses, J. Anal. At. Spectrom. 20 (2005) 901–906.
[66] J. Kosler, R.B. Pedersen, C. Kruber, P.J. Sylvester, Analysis of Fe isotopes in sulfides and iron meteorites by laser ablation high-mass resolution multi-collector ICP mass spectrometry, J. Anal. At. Spectrom. 20 (2005) 192–199.
[67] L.V. Zhigilei, D.S. Ivanov, E. Leveugle, B. Sadigh, E.M. Bringa, Computer modeling of laser melting and spallation of metal target, High-Power Laser Ablation V, Proc. SPIE 5448 (2004) 505–519.
[68] Handbook of Chemistry and Physics, 83 ed., CRC Press.
[69] D. Bleiner, Ph. Gasser, Structural features of laser ablation particulate from Si target, as revealed by focused ion beam technology, Appl. Phys. A Mater. Sci. Process. 79 (2004) 1019–1022.